GEOPHYSICS

Delayed submarine caldera subsidence creates extreme tsunami hazard

Shane J. Cronin[1]*, Bastian Steinke[1], Jose C. Borrero[2], Emile A. Okal[3], Marta Ribó[4], Jie Wu[1], James D. L. White[5], Marco Brenna[5], Joali Paredes-Mariño[1], Mila Huebsch[1], Rachael Baxter[5], Ulrich Speidel[6], Alexa R. Van Eaton[7], Larry G. Mastin[7], Michael A. Clare[8], Isobel A. Yeo[8], James E. Hunt[8], Jacob Nash[8], James B. Garvin[9], Rennie Vaiomounga[10], Taaniela Kula[10], Sung-Hyun Park[11]

The 2022 Hunga volcano eruption generated one of the largest and most destructive volcanic tsunamis ever recorded. We interpret the timing, nature and relative hazard of volcanic-tsunamigenic processes by combining geophysical, oceanographic, atmospheric, and eye-witness observations of this event. Hydro-acoustic signal (*T* waves) detected on seismic stations up to 2600 km away provided a key to discerning tsunami triggers from explosions, volcanic mass flows, and caldera subsidence. The largest tsunami was generated by the first of at least two sudden caldera-subsidence events. This occurred 1 hour after globally detected explosions that produced smaller tsunami. Our results provide rare insights into the rates of caldera subsidence and highlight the complex multiple sources of tsunamis resulting from eruptions of oceanic volcanoes.

INTRODUCTION

Isolated eruptions from oceanic and submarine volcanoes are rare to observe directly and difficult to monitor instrumentally. Despite this, the VEI 6, 15 January 2022 eruption of Hunga volcano (Kingdom of Tonga, SW Pacific; Fig. 1) is one of the best recorded, large-scale emergent to submarine eruptive events known. The eruption has already extended our knowledge of volcanic processes through a series of superlatives, including: the highest (and widest) eruption plume ever recorded (*1*, *2*); the greatest rates of lightning ever recorded (>2600 flashes min^{-1}) (*3*); unique globe-encircling atmospheric waves coupled to the ocean surface (*4*–*7*); the fastest eruption-fed density currents (submarine mass flows) ever documented (*8*); rapid formation of a ~860-m-deep and 3.6-km-wide caldera of ~6.85 km^3 volume (*9*–*11*), and globally dispersed volcanic tsunami (*12*–*14*), including an unusually large and catastrophic event (*15*, *16*).

Few volcanic tsunami are recorded and even fewer with submarine triggers (*17*). Krakatoa's 1883 VEI 6 eruption produced similar near- and far-field effects to Hunga (*18*, *19*), with the largest tsunami associated with pyroclastic density currents (PDCs) entering the ocean (*20*, *21*). The 1952 Myojin-Sho (Japan) and 1996 Karymskoye Lake (Russia) eruptions generated tsunami via submarine explosions, and Ritter Island (Papua New Guinea) via submarine flank collapse in 1888 (*17*, *22*–*24*). Hunga's largely submerged 1800-m-high edifice produced multiple caldera-forming eruptions in the last few thousand years and its potential for large-scale eruptions was recognized (*25*, *26*). Small deep calderas such as Hunga (Fig. 1B) (*8*, *11*) form mainly by piston-style collapse (*27*). While calderas may subside gradually (*28*–*30*), rapid and large submarine caldera collapses are likely tsunamigenic (*21*, *31*, *32*). Caldera subsidence during eruptions is also associated with other tsunamigenic processes, such as PDCs, eruption-fed submarine currents or mass flows, landslides and explosions (*17*, *21*, *33*). Because of few well-observed examples of volcanic-tsunami genesis, their threats are poorly quantified and they are not included in automated global warning systems (*21*).

Near-field measurements of submarine and small-island eruptions are rare, because isolated oceanic volcanoes lie typically far from land-based seismic networks and ocean-bottom seismometers are sparse. Far-field seismic recordings do not capture near-surface volcanic processes well, due to the attenuation of high-frequency seismic energy [e.g., (*34*)]. The closest stations to the 2022 Hunga eruption were 750 km away (Fig. 1A). At such distances, only major explosions and the highest energy, magma-tectonic processes are recorded seismically (*35*). On the other hand, submarine mass-movement processes may directly radiate energy into seawater, generating hydro-acoustic energy (*36*). Hydro-acoustic waves travel efficiently in the SOFAR (Sound Fixing And Ranging) channel (*37*), at water depths of 600 to 1800 m. These are converted into seismic energy as they encounter land. The energy that passes through the SOFAR channel travels at <30% of the celerity of *P* and *S* seismic phases [i.e., 1.49 km s^{-1} in the Pacific Ocean; (*36*)], hence the term, tertiary seismic phase or *T* waves (*38*, *39*). Travel times of *T* waves can be altered by local bathymetry, repetitive conversion between hydro-acoustic and seismic phases, and heterogeneities in the water column (*39*, *40*). By providing insight into the high-frequency part of the seismic spectrum (typically 2 to 10 Hz), *T* waves may reveal tsunamigenic sources violating seismic scaling laws, which can consist either of anomalously slow seismic events [i.e., "tsunami earthquakes" (*41*)], or landslides and volcanic eruptions (*42*–*46*).

Combining seismic, hydro-acoustic, oceanographic, atmospheric, and eye-witness data from the 15 January 2022 Hunga eruption (Fig. 2), we provide an integrated overview of the ~11-hour-long

[1]School of Environment, The University of Auckland, Auckland 1010, New Zealand. [2]Department of Civil and Environmental Engineering, University of Southern California, Los Angeles, CA 90089-2531, USA. [3]Department of Earth and Planetary Sciences, Northwestern University, Evanston, IL 60208, USA. [4]School of Science, Auckland University of Technology, Auckland 1010, New Zealand. [5]Department of Geology, University of Otago, Dunedin 9054, New Zealand. [6]School of Computer Science, The University of Auckland, Auckland 1010, New Zealand. [7]US Geological Survey, Cascades Volcano Observatory, Vancouver, WA 98683, USA. [8]National Oceanography Centre, Southampton SO14 3ZH, UK. [9]NASA Goddard Flight Centre, Greenbelt, MD 20771, USA. [10]Geology Unit, Natural Resources Division, Ministry of Lands and Resources, Nuku'alofa, Tonga. [11]Korea Polar Research Institute, Incheon 21990, Republic of Korea.
*Corresponding author. Email: s.cronin@auckland.ac.nz

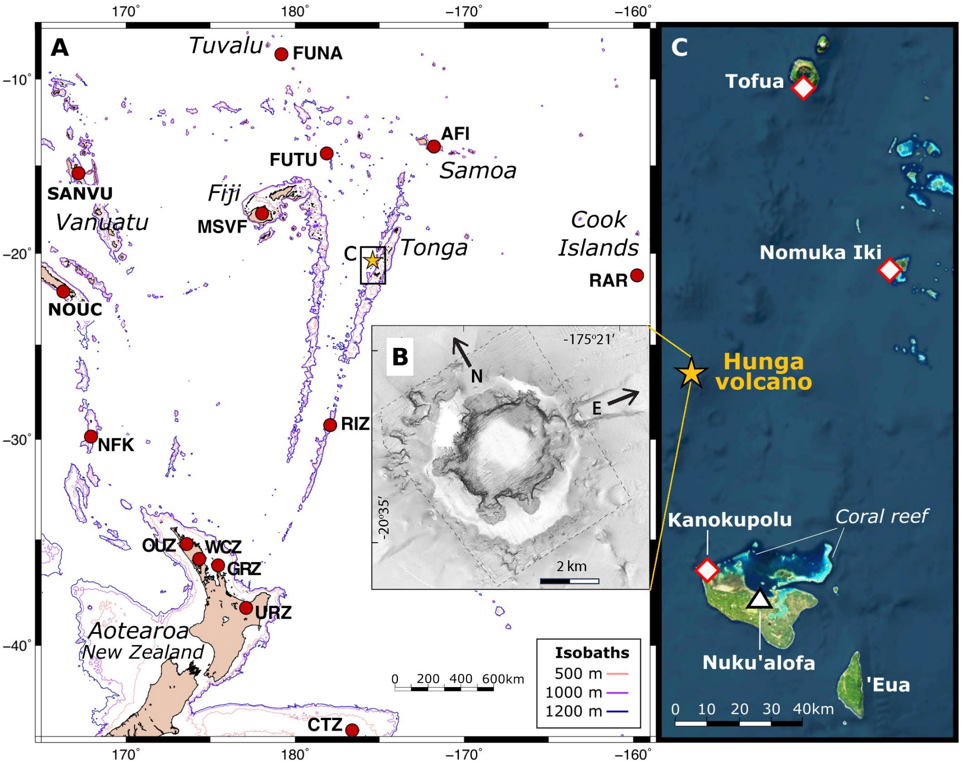

Fig. 1. Maps of Hunga volcano and surrounds. (**A**) Map of part of the SW Pacific showing seismic sensors (red circles) included in this analysis and the major bathymetric features relevant for hydro-acoustic sound (*T* wave) transmission. Station details are listed in table S1. (**B**) Shaded slope map of the Hunga caldera posteruption. The deepest flank channels that focused eruption-fed-density currents are annotated with arrows and labeled N and E. (**C**) Map of Tongan islands nearest to Hunga volcano. Nuku'alofa Harbour (tide gauge and weather station), on Tongatapu Island is marked by a white triangle. The diamonds indicate the locations of peak run-up heights from the largest tsunami: 18 m at Kanokupolu (05:45 UTC) (western Tongatapu), 21 m at Nomuka-iki Island (~05:50), and up to 40 m on Tofua Island (time unreported).

eruption and isolate the most important volcano-oceanographic processes. In particular, we document the rare case of a submarine caldera subsidence event and quantify its timing, duration, and influence on tsunami generation and volcanic dynamics. Through this work we show how *T* waves can be used to distinguish between eruption-fed density currents and caldera-collapses. Below, we describe the distinct eruption phases including escalation to peak intensity, plume foundering, and coincident catastrophic tsunami generation.

RESULTS

Eruption escalation to peak intensity (04:00 to 04:40)

Following several weeks of intermittent Surtseyan eruptions (*47*), the climactic Hunga eruption spanned from ~04:00 to 15:12 universal time coordinated (UTC) on 15 January 2022 (*3*) (local time is UTC +13 hours, all times are reported in UTC). The first plume visible on satellite imagery was at 03.00 (Fig. 2A) (*3*). The largest seismically recorded explosion events occurred at ~04:15 and ~04:25 [with equivalent seismic energy up to M5.8 (*48*)]. Each explosion generated a tsunami (Fig. 2C) with 1- to 4-m run-up that reached Kanokupolu on western Tongatapu (Fig. 1C; ~58 km travel distance), after 8 to 10 min travel time (*15*, *16*). Waves from the same explosion events were registered on a tide gauge in the nation's capital city Nuku'alofa (~69 km travel distance) around 15 min later (Fig. 1C). The small artificial harbor housing the tide gauge is subject to overflow and peak wave attenuation. Security camera footage from Nuku'alofa waterfront confirms two of the many tsunami wave arrivals at ~04:45 and ~05:17, before power failure. Slower tsunami arrival at Nukualofa is due to the longer travel distance and the waves traversing a ~15-km-wide shallow bench (<30 m-deep) before arrival (fig. S1) (*15*, *16*). Global air pressure oscillations during this time also generated distal deadly tsunami across the wider Pacific Ocean (*4*, *13*, *49*, *50*).

Accompanying explosions between 04:15 and 04:25, the Hunga eruption plume rapidly rose, expanded and generated high-intensity lightning, until the plume top peaked at ~04:40 (Fig. 2A and fig. S2) (*2*, *3*). Plume growth was accompanied by increasing mass eruption rate (MER), as inferred from increasing energy of eruption-related seismicity (at frequencies <0.2 Hz at the closest station ~750 km away; Fig. 2, D and E). Negative spikes in air pressure were recorded on Tongatapu (Fig. 2B), indicating ingestion of surface air into the rising plume, associated with pulsing in eruption energy. High lightning rates ensued due to the dominance of steam in the plume, which converts to ice particles above 9 km in elevation (fig. S2) (*3*).

Contrasting with a typical Plinian eruption column fed by gas expansion of magma, the Hunga plume was driven by magma volatilizing seawater (*51*), with rates of thermal input and steam production similar to the heat flux from erupting magma (*52*). The plume-top showed little variability from ~04:40 until 05:30, but concurrently the <0.2 Hz seismicity and lightning rates waned (Fig. 2E). The eruption vent was likely near the NW caldera rim,

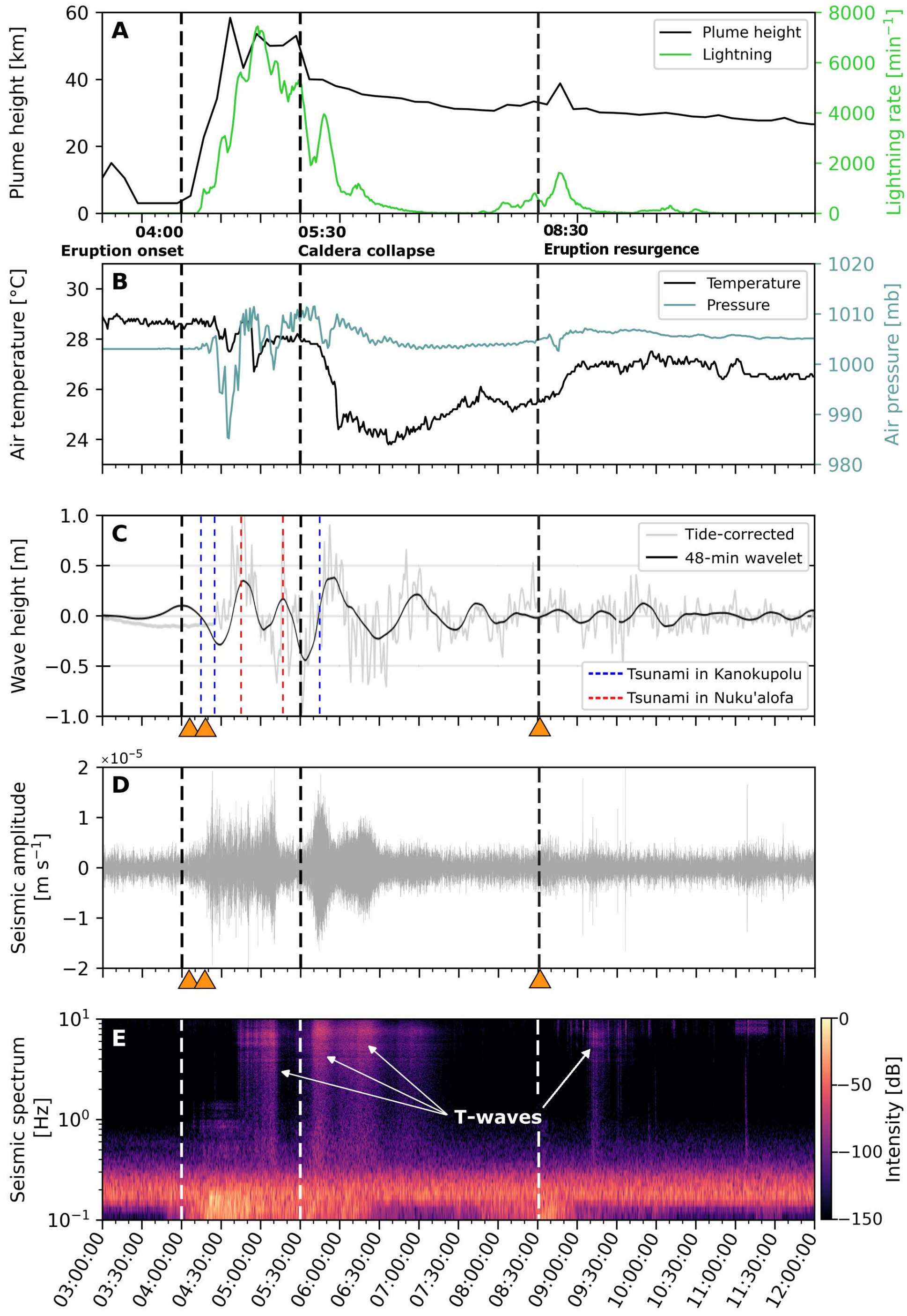

Fig. 2. Multiproxy timeline of the 15 January 2022 Hunga eruption. (**A**) Eruption plume height and lightning rate (*3*). Timing of eruption onset and caldera collapse and late eruption resurgence are marked by vertical black dashed lines that pass into panels below. (**B**) Air temperature and pressure and (**C**) Tide gauge recorded at Nuku'alofa Harbor on Tongatapu Island. Tide-corrected water level plotted in gray, with a 48-min-period wavelet decomposition of the tsunami in black. Timing of individual waves captured on security footage in Nuku'alofa is indicated by vertical red dashed lines. Tsunami peaks witnessed at Kanokupolu (west Tongatapu) are marked by the first two blue dashed lines, with the last blue line marking the time of destruction of the Kanokupolu communication tower. Yellow triangles at the base of the plot mark the timing of distinct major atmospheric explosions as recorded by Tarumi and Yoshizawa (*48*). (**D**) Amplitude and (**E**) spectral characteristics of seismic records from station MSVF, located in Fiji, 757 km from Hunga. Low-frequency energy (<0.2 Hz) is interpreted as volcanic eruption seismicity, while major higher frequency features (>1 Hz, from 04:40 a.m. UTC onward, labeled "*T* waves") are interpreted as hydro-acoustic signal.

where precursory 2021–2022 eruptions (*47*) and 2014–2015 eruptions occurred (*26*).

Eruption-fed mass flows (04:00 to 4:40)

The arrival of higher frequency (1 to 10 Hz) signals at station MSVF in Fiji from ~04:40 (Fig. 2E) evidence hydro-acoustic energy dispersal from Hunga volcano, because volcano-seismic signals are attenuated for this frequency range. This was confirmed by checking the onset times of correlative signals at other land-based stations within 1000 km of the volcano. Stations FUTU, MSVF, and AFI (Fig. 1) record two *T*-wave arrivals in the period from 04:00 to 05:15 (fig. S3). More distal stations only record one or the other event, while sensors >2000 km away do not record them at all. We correlate these hydro-acoustic signals to the formation of eruption-fed submarine mass flows (*33*). Eruption column unsteadiness and pyroclastic surges (water-rich PDCs) travelling out to ~6 km radius are noted in time-lapse images of the eruption (fig. S2). Initial eruption-fed mass flows were likely channeled into low points on the volcano rim leading to major channels on the northern and eastern volcano flanks (Fig. 1). Bathymetric mapping revealed substantial erosion of these channels and the destruction of sea-floor cables, 20 km east of the volcano (domestic cable) at 04:30 and ~60 km south of the volcano (international cable) at 05:44 (*8*). Numerical models and sea-floor deposit mapping (*8*, *10*, *53*) conclude that at least 10 km^3 of eruption deposits were emplaced over 100 km from the volcano. Backtracking *T*-wave arrival times from FUTU, MSVF, AFI, and RAR stations (fig. S3) shows that the earliest eruption-fed mass flows were initiated at ~04:00 and corresponded with explosions 1 and 2 reported in Purkis *et al.* (*16*). This suggests a minimum average flow front velocity of ~11 m s^{-1} to reach the domestic cable. Clare *et al.* (*8*) estimated velocities of 17.5 to 34.2 m s^{-1} based on triggering by the largest explosions between 4:15 and 4:25, but there is no *T*-wave signal consistent with eruption-fed mass flows triggered in this interval. A second and larger *T*-phase event initiated at 04:40 (±5 min) and coincided with the peak MER of the eruption. The longer duration and wider dispersal of this signal (Fig. 2E and fig. S3) suggest more widespread eruption-fed mass flows radiated down all volcano flanks during the MER climax (*8*, *10*). Despite this, the *T* wave is mainly recorded on stations <1000 km distance, as well as RAR at 1625 km to the east (fig. S3). Flows generated during the 04:40 episode likely traveled at an average of 15.6 m s^{-1} to reach the international cable [slightly faster than the 13.9 m s^{-1} estimated by Clare *et al.* (*8*)].

Postclimax plume foundering (~05:30)

Approximately 1.5 hours after the eruption onset (between satellite passes at 05:27 and 05:37; Fig. 2A), the plume top declined from >53 to 40 km, along with a decrease in lightning (*3*). At 05:40, a brief lightning peak occurred along with a small pressure decrease ($\Delta_P = 5$ mb) on Tongatapu (~70 km SE) (Fig. 2, A and B). By 05:45 air temperature on Tongatapu sharply dropped ($\Delta_T = 4$°C) for several hours before returning to normal later that night (local time) (Fig. 2B). Surface arrival of the descending cold plume explains the magnitude of temperature drop and a subtle increase in air pressure (Fig. 2B), which is much greater than the $\Delta_T = 1$°C decrease associated with the expanding umbrella plume blocking sunlight over Tongatapu between 04:30 and 05:30.

The collapse of an eruption plume during an explosive eruption can be caused by a rapid decrease in MER, sudden widening of the vent zone, caldera subsidence, and/or other dynamic factors [e.g., (*54*–*57*)]. In humid eruption plumes, heavy downdrafts of ice and rain may also promote plume collapse (*58*). Seismic amplitude and energy in the <0.2 Hz frequency range (Fig. 2, D and E) gradually decreased at MSVF from 05:15 onward, reaching near pre-eruption levels by 06:30. A smaller surge in <0.2 Hz seismicity between 07:45 to 09:00 is associated with a late explosion at 08:30 (*48*), and a short-lived plume resurgence >35 km high (Fig. 2A). Another minor plume fluctuation event at 14:00 preceded the eruption ceasing at 15:12 (*3*). There is no evidence of a sudden drop in MER coinciding with plume collapse, so other causal mechanisms are needed.

Peak local tsunami arrival (~05:45)

The devastating inundation and destruction of coastal settlements on Tongatapu occurred at the same time as the loss of a weather station on the Kanokupolu Peninsula (Fig. 1) that sent its last (hourly) data packet at 05:00 (*15*). The weather station and its associated telecommunications tower are 180 m inland at ~13 m elevation and were not affected by earlier smaller tsunami as residents evacuated. The station was ultimately ripped from its foundations and parts were found hanging from a tree branch 5 m above ground level ~260 m inland. The Tonga Communications Corporation determined that data traffic through the tower ceased at 05:45:24, indicating the time of its destruction. An 80-min delay between the first tsunami waves and the most catastrophic local tsunami is also supported by eyewitnesses' accounts from evacuees in Kanokupolu and islands ~80 km north of Hunga. Tsunami between 04:15 and 04:25, with 1- to 4-m run-ups in Kanokupolu, are well-linked to explosions ~8 to 12 min earlier at the volcano (*15*, *16*). However, no large explosions occurred at a time required (~05:30 to 05:35) to generate the catastrophic tsunami arriving at ~05:45. Thus another source mechanism is needed.

DISCUSSION

Relating caldera subsidence to plume destabilization and peak local tsunami

As the eruption MER diminished from ~05:15 onward (shown by the <0.2 Hz seismicity at MSVF and other nearby stations), a large and persistent high-energy >1 to 10 Hz signal arrived at 05:38 (Fig. 2E). We interpret this as hydro-acoustic energy (i.e., a *T* wave), generated by a much stronger submarine signal source than previously recorded at Hunga. We identify this *T* wave in the seismic records of 14 SW Pacific sensors with a coherent pattern (Fig. 3 and fig. S4). Of these, arrivals at 12 stations suggest a common source event at Hunga at ~05:28 (Fig. 3 and table S1). Observed phase delays are consistent with distance to 10 stations (Fig. 3 and table S1), while station CTZ shows extremely slow and station FUNA an early *T*-wave arrival that do not match the anticipated origin time of the signal. The onset is obscured by noise at station NOUC, and the *T* wave is weak at RIZ. Stations OUZ and WCZ, despite being 1951 and 1978 km from Hunga, respectively, show an expected *T*-wave arrival time.

T waves result from efficient release of acoustic energy into the SOFAR channel at 600 to 1800 m below the water surface. Subsidence of a ~4-km-diameter cylindrical rock mass from a pre-eruption level of 0 to 200 m below sea level to >860 m depth is evidenced by seafloor mapping at the summit of Hunga volcano before and after the eruption (*8*–*11*). Submarine caldera subsidence involves intense shearing along ring faults and associated reconfiguration of the

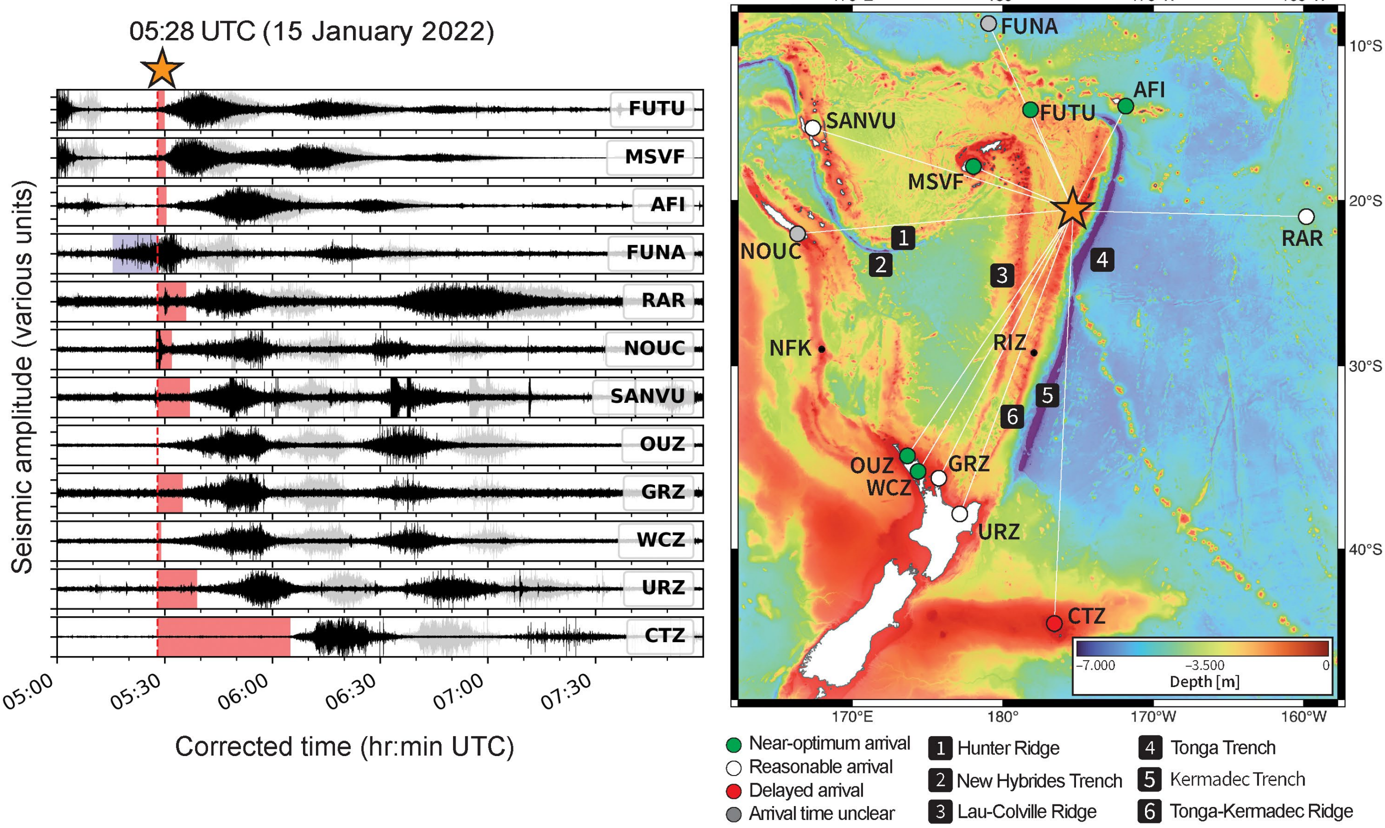

Fig. 3. Seismic spectra of the most energetic *T* wave of the Hunga eruption over 12 of the 14 SW Pacific stations at distances between ~750 and 2600 km. Station details and arrival times in table S1, and full spectra in fig. S4. Note that RIZ is too noisy to isolate the signal onset and NFK has an incomplete record. The signals are time-corrected and stacked with respect to the theoretical arrival time of the first detectable signal onset (*T*-wave arrival). Back-projected travel times from stations indicate an origin event starting at 05:28 at Hunga volcano (orange star and vertical dashed line). The difference between expected and actual arrival time is indicated via a color code within location markers (table S1) with 1 to 2 min as near-optimum arrival (green markers), 5 to 11 min reasonable arrival due to bathymetric obstructions (white markers) and red for exceptional delay, which cannot be explained readily by direct ray path bathymetry (red marker). Uncertain arrivals include NOUC where the arrival time is obscured by a sharp transient signal and at FUNA where the signal apparently arrives too early (gray markers). Major bathymetric features affecting *T*-wave travel are marked in numbered black squares.

shallow vent structures as well as multiple smaller-scale landslides. Such underwater mass movement generates intense hydroacoustic energy. The ~05:28-generated *T* wave has a duration of 10 to 15 min at stations north of the volcano (MSVF and URZ; Fig. 3 and fig. S4), and ~30 min at more distant stations in other directions. The strongest signal lasts only ~5 min, indicating a probable timescale for a caldera subsidence event. Over the next hours, one or two less-energetic *T* waves are recorded by most stations, suggesting stepwise caldera collapse (Fig. 3 and fig. S4). Backtracking the second *T* wave suggests an onset time of the second caldera subsidence event at ~06:06 (figs. S5 and S6 and table S2).

The coincidence of eruption plume breakdown with gradually waning MER, but high-energy *T* waves, implies that plume collapse was caused by rearrangement and defocusing of the vent, rather than meteorological or internal-plume processes. Rapid caldera subsidence substantially alters the dynamics of an eruption and redistributes mass discharge around multiple vents on the caldera rim and ring faults (*59*, *60*). In Plinian eruptions, this leads to reduced discharge velocity and gas-thrust height, and increased bulk density within the vertical plume (*56*, *61*). In the steam-fueled thermal Hunga plume (*52*), a rapid defocusing of steam production would have the same effect. *Plumeria* model results show that the gas-ash mixture within the Hunga plume rose to 50 km in 4.2 to 4.7 min, much faster than normal Plinian volcanic plumes (*52*). Thus, the plume collapse is also likely at the faster end of the range of the 5 to 15 min modeled by Van Eaton *et al.* (*58*) for high Plinian plume collapses. Satellite evidence of plume foundering at Hunga thus suggests caldera subsidence occurred between ~05:20 and 05:30 (Fig. 2A).

A rapid caldera subsidence event also explains the generation of the peak tsunami. This process may cause a negative initial tsunami wave, followed by a positive one (*62*–*64*). Thus, the Kanokupolu tsunami arrival may have been several minutes before the cell-tower destruction at 05:45, placing the triggering event closer to 05:30. Bringing together all available observations, the initiation of the main episode of caldera subsidence converges at 05:28 to 5:30. At 05:30 a shallow M4.7 earthquake was recorded near the volcano [USGS Earthquake Catalogue (*35*)], which may be related to caldera subsidence or simply coincident.

This largest local tsunami of the eruption sequence caused an almost radial pattern of >18 to 40 m run-ups within 100 km from source (Fig. 1C) (*15*, *16*). By comparison, the 2018 Krakatau tsunami had already decayed to <3 to 9 m run-ups by 20 to 50 km from source and was strongly directional (*65*). A corelative set of waves is recorded on the Nuku'alofa gauge at ~05:55 (Fig. 2C), consistent with time delays between the two stations in the earlier tsunami. Approximate arrival times for the largest tsunami at Nomuka-iki (~75 km ENE) is estimated by eyewitnesses at ~05:50, who had evacuated from the coast under darkness and heavy ash fall. Peak wave timings at all these sites confirm that the tsunami was triggered between 05:28 and 05:35 at Hunga. Subsequent caldera subsidence events recorded by *T* waves from ~06:06 onward may be responsible for later, smaller tsunami peaks recorded at Nuku'alofa (Fig. 2C).

Insights into submarine volcanic processes using *T* waves

Our results highlight that two types of long-range hydroacoustic signal were generated at Hunga (Fig. 4 and fig. S7); (A) weaker *T* waves mainly noted at closer stations (750–830 km), or in specific directions; and (B) stronger *T* waves that are traceable in all directions and to distances >2000 km. Type A signals include unsteady pulses of 1 to 5 min duration and may only span 5 to 10 Hz, while those of type B are steadier and more evenly span the 1 to 10 Hz range (Fig. 2E and figs. S3 and S7). On the basis of plume observations (fig. S2), we associate Type A *T*-wave signals with the generation of PDC dispersal and eruption-fed submarine mass flows. Submarine mass flows from all sources generate a strong directionality in *T* waves (*42*, *66*). At Hunga, unsteady, pulsing signals likely reflect repeated collapsing eruption jets that along with radiating pyroclastic surges (steam/water rich PDCs) emplace pyroclastic material on the steep volcanic flanks to feed energetic and erosive (i.e., noisy) submarine currents (Fig. 4, A and B). These are likely concentrated through low points on the caldera rim and into channels on the N and E volcano flanks (*8*). Eruptions with magma-surface water interaction are notably unsteady, with repeating pulses of particle-rich jets, and wet surges that radiate hundreds to thousands of meters (*67*–*70*). Eye-witness observations and videos of Hunga eruptions on 30 December 2021 show radiating pyroclastic surges radiated out 1 km from collapsing jets, increasing to 2.5 km radius on 14 January 2022, and photographs suggest these extended at least 6 km by 04:25 on 15 January 2022. Once generated, submarine mass flows are thin and spread over wide areas of seafloor. Thus, the sources of hydroacoustic signals are weak, dispersed, and mobile. Flow

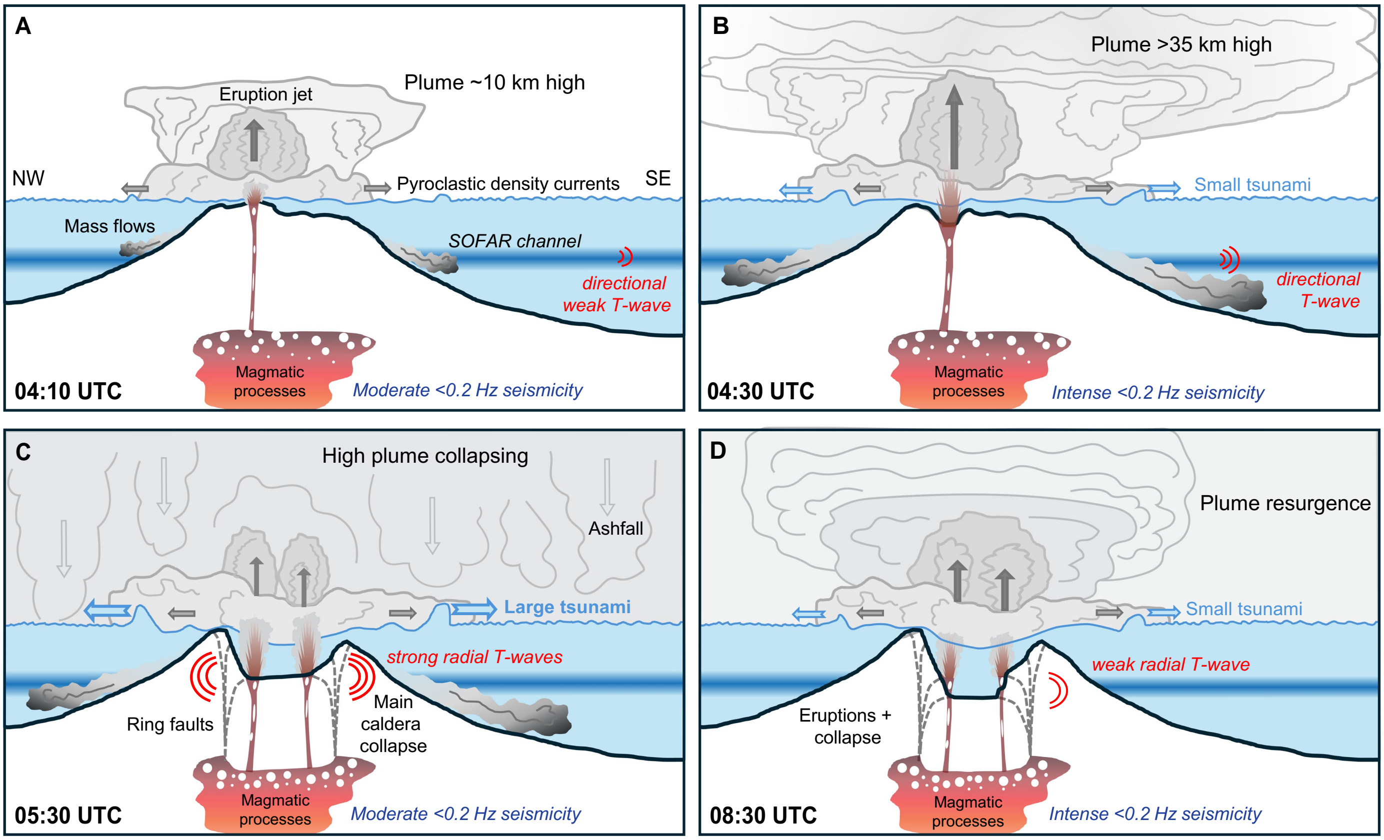

Fig. 4. Key stages of the Hunga eruption timeline and sources of *T*-waves and tsunami. Horizontal and vertical scale is based off the bathymetric profile of Hunga volcano. The low-velocity zone of the SOFAR channel center is ~750 m deep in the Pacific Ocean and acts as a wave guide. Magmatic and eruptive processes are generally recorded as low-frequency (<0.2 Hz) energy on seismic stations >750 km distance. (**A**) Early eruption stages (started at 04:00 UTC) with PDCs radiating from the main (northern) vent up to 2 km. Submarine mass flows to the N and E generate small *T*-wave signals on close stations (figs. S3 and S7). (**B**) Rise to peak eruption intensity, with plume reaching maximum height at 04:30 UTC. PDCs radiate at least 6 km across the water (fig. S2) and large pulsing submarine mass flows result from eruption-fed density currents. Tsunami (locally <3-m run-up) are generated by explosions. (**C**) Caldera collapse causes foundering of eruption plume and slip along caldera ring faults generates persistent strong *T* waves (Fig. 2 and fig. S4) on all stations including at distances >1900 km. The largest local tsunami is generated by this caldera collapse (run-up 18 to 40 m at 60 to 100 km from source). (**D**) A late eruption pulse from 08:30 UTC causes a brief plume resurgence and generates a short *T* wave signal and a small tsunami.

channeling directs energy in the direction of travel and *T* waves from submarine landslides and explosions feature strong directionality [e.g., (*42*, *66*)]. This explains why only the closest stations to the N and E record the eruption-fed currents at Hunga.

The large magnitude and longer-range type B hydroacoustic signals represent a source process with far more efficient transfer of energy from the volcano into the surrounding ocean, such as deep landsliding or shallow fault motion (i.e., without major tele-seismic energy dispersal). High-energy signals were generated by deep slumping events compared to shallower landslides at Kick-'em-Jenny Volcano (*66*). Hence, a probable source for *T*-wave signals of Type B at Hunga is shallow fault motion and landsliding during subsidence of the submarine caldera (Fig. 4C). There was at least 860 m of cumulative vertical offset on ring-faults around a ~4-km-diameter caldera. This represents a large surface area of vertical shear, with additional shallow faults and associated landslides likely contributing to submarine energy. Multiple *T* waves suggest that caldera subsidence was stepwise, although the amplitude of the first collapse-generated signal was the strongest. The Hunga edifice depth and caldera subsidence down to ~860 m below sea level was also well aligned to the SOFAR channel (Fig. 4C), thus maximizing the efficiency of *T*-wave transmission.

Hydro-acoustic waves experience little attenuation, which makes them reliable suppliers of information over long distances (*71*, *72*). The 05:28-origin *T* wave from Hunga, however, arrived at stations between 1 and 11 min later than the theoretical travel time, with one extreme case 37 min late (Fig. 3, fig. S4, and table S1). *T*-wave propagation in the SOFAR channel may be obstructed by seamounts and ridges, delaying signal arrivals due to reflection and path diversion around bathymetric obstacles. Direct signal paths to recording stations from Hunga include major bathymetric features within the SOFAR channel (fig. S8), although these are not always reflected in travel time delays. At SANVU, a slow arrival could be due to a wave path diverting around a shallow ridge (Fig. 3). In New Zealand, the northernmost OUZ and WCZ stations record the peak *T* wave almost simultaneously with little delay, while farther south GRZ, URZ show increasing delays. These delays could be due to wave reflection and slowing while travelling subparallel to the Tonga-Kermadec Ridge and the Kermadec Trench. For CTZ, a delay of 37 min is too long to be explained by simple deceleration of hydroacoustic energy transmission and instead suggests a diverted raypath (e.g., around the continental shelf of New Zealand). Shallow onset slopes (e.g., continental shelves) delay *T* waves more effectively than steep slopes (*36*, *39*), which may also explain some of the delay at CTZ. By contrast, *T* waves crossing perpendicularly through steep ridges or trenches (e.g., to RAR, E of Hunga) were unaffected. A possible 06:06 origin *T* wave from Hunga is harder to detect clear onsets due to signal overlap, but it appears to show similar behaviors to first T wave in stations to the N and W but much greater delays than expected in S and E stations. This may suggest that these represent two separate source events firstly in the NW caldera at 06:06 and then ~15 min later in the SE caldera (figs. S5 and S6 and table S2) (*36*, *39*).

Hazard lessons

The 15 January 2022 Hunga eruption began at 04:00 with weak *T* waves on the closest seismic stations (<750 km), evidencing eruption-fed submarine mass flows channeled to the north and east from the NW-caldera rim vent (Fig. 4A). These traveled >11 m s^{-1} eastward to destroy a submarine cable by 04:30. As the eruption plume transformed and grew during a series of major atmospheric explosions between 04:15 and 04:25, large explosion-related tsunamis were generated (run-up 1 to 4 m within 100 km from source), but no sustained *T* waves were generated. However, once the mass-eruption-rate reached its peak between 04:40 and 05:05 high-energy eruption-fed density currents were again generated by jetting and PDCs depositing debris rapidly onto the steep volcano flanks (Fig. 4B). Strong *T* waves are recorded down-slope of northern and eastern channels (fig. S3) and the submarine mass flows traveled >15.6 m s^{-1} to damage a submarine cable ~60 km south of the volcano.

Despite the size of this eruption, it only became locally catastrophic once the ~4-km-diameter caldera suddenly subsided (Fig. 4C). The first and largest subsidence event of a series of stepwise failures began at 05:28 and generated one of the largest volcanic-induced tsunamis ever recorded, with run-ups reaching >18 to 40 m at up to 100 km from source. Caldera subsidence also caused the coincident rapid foundering of the eruption plume. The first caldera collapse released its strongest energy during a period of ~5 min to generate high-energy *T* waves captured on 14 SW Pacific seismic stations up to 2600 km away. At least two subsequent subsidence events produced similar high-energy *T* waves, with a later eruption pulse associated with one of them at ~08:30 (Figs. 2A and 4D).

One of the most remarkable implications of this study is that sudden failures along ring faults and caldera subsidence caused the largest and most destructive volcanic tsunami recorded in the last 140 years. Caldera collapse was weakly detected seismically, compared to the large atmospheric explosions of the early eruption [at 04:15 to ~04:25 (*13*)]. The subsidence began as eruption energy waned, ~30 min after the eruption-rate climax. Because of the generally short wavelengths of this type of tsunami source, it likely dispersed quickly, explaining why the largest amplitudes were confined to within 150 km. In a comparative case, the 2018 Krakatau tsunamigenic flank collapse may have preceded the atmospheric explosion and infrasound waves by about 7 min (*73*). These two examples show that volcanogenic tsunami may have highly unpredictable triggering processes and timing. The Hunga case reaffirms that deadly tsunami hazard may be associated with processes ancillary to a catastrophic eruption. In this case, the caldera collapse produced a tsunami on nearby islands far larger than the major explosions. Because the collapse and tsunami trigger is from an already unstable system, predicting its timing is difficult, adding uncertainty to the hazard. Furthermore, in order to adequately forecast wave dynamics of volcanic tsunami, multiple overlapping generation processes must be considered, with variable timing as well as coincidence of source processes highly likely.

Despite extreme hazards posed by numerous oceanic island and submarine volcanoes, they remain challenging to monitor, especially because eruptions show large disparities in the sequence and nature of events. *T* waves offer a potential for volcanic tsunami alerting, but because *T* waves are intrinsically high-frequency (>2 Hz), their amplitude can provide deceptive estimates of the long-period characteristics of sources of tsunami excitation (*39*, *43*). However, they may help detect underwater sources such as eruption-related mass flows, notably because they obey different scaling laws, as evidenced by the 1998 Papua New Guinea tsunami (*74*) or during recent volcanic crises at Sofu Seamount (*75*). In the case of the Hunga event, the caldera-collapse demonstrates a previously unrecognized *T* wave source, intermediate between a submarine landslide and an earthquake. Shallow slip during caldera collapse likely occurs by a series of small (and possibly seismically slow), successive slips on separate parts of the ring fault system around the caldera over a period of minutes to hours.

Our findings highlight the diversity of *T* waves and thus their potential utility in monitoring difficult to access distal submarine volcanic eruptions. We show that submarine caldera collapse is a highly effective mechanism for tsunami generation and that *T* waves, which travel ~7 to 10 times faster than tsunami, have great potential for early warning of tsunami generated by major submarine mass flows and caldera collapse.

Methods

Tsunami arrival times and eye-witness accounts of eruption phenomena were assembled during a 3-month field period in Tonga, with interviews carried out by S.J.C. and J.C.B. Photographic and video footage of the eruption events with time stamps were used to identify key moments during the eruption as reported in Borrero *et al.* (*15*) and Clare *et al.* (*8*), with further observations of tsunami arrival times and communication failures added in this work. Telecommunications tower data were provided by Tonga Communications Corporation. Bathymetric profiles to Kanokupolu and Nuku'alofa (fig. S1) were generated from GEBCO (*76*) and Mitchel *et al.* (*77*) bathymetry maps via Q-GIS software.

Data on eruption plume dimensions and volcanic lightning in Fig. 2A were reported by Van Eaton *et al.* (*3*). The umbrella cloud height was estimated via a dual-satellite configuration. Lightning activity was tracked using ground-based sensors. The lightning time series data were binned into nonoverlapping 1-min intervals, returning the number of registered pulses per minute. Only pulses in close proximity to the center of the eruption column (<20 km distance) were considered because the high flash rates saturated one of the sensors, leading to less reliable pulse detection at greater distances (*3*).

The first available eye-witness images of the eruption are at 04:11 UTC and the last-available showing the whole plume was at 04:30 UTC. A set of images (fig. S2) was captured from short video clips made by Connor Campbell from a single location on the waterfront in western Nukualofa, northern Tongatapu (21°7.475′S, 175°13.204′W), 66.5 km from Hunga volcano. Following interviews with Susie and Connor Campbell by S.J.C., timestamps on the original files were used to identify photograph times (±10 s) and any changes in focal length to render the same perspective (at the distance of the plume) for each image. Brightness/contrast of the original bright afternoon images (clear skies ~17 hours local time) was modified to highlight features of the eruption plume.

Meteorological parameters, air temperature and air pressure (Fig. 2B), and wave amplitude data (Fig. 2C) were recorded by a meteorological station and a tide gauge, respectively, both located ~69 km SE of Hunga volcano in the Nuku'alofa Harbor (*15*) and supplied by the Tonga Meteorological Service. Subtracting the tidal range from the raw gauge data reveals the amplitude of incoming and reflected tsunami waves within the harbor. The raw data were sampled at one datapoint per minute. Wavelet decomposition was performed on the record for a range of frequencies. The 48-min-period wavelet plot described the main background pattern of the signal well and likely indicates the structure of the main tsunami wave train. Security camera footage for tsunami wave arrival timing (Fig. 2C) was provided by Susie Cambell from Sopu (4 km west of the harbor) and the Billfish Bar (21°8.432′S, 175°10.820′W), adjacent to the Nuku'alofa harbor.

Seismic records were extracted from the vertical component of short-period station MSVF (40 Hz sampling frequency) via the FDSN server. The station is located in Fiji, approximately 750 km WNW of the volcano, and is one of the closest active stations at the time of the eruption. We removed the instrument response from the raw data before applying a Butterworth filter between 0.1 and 10 Hz. The associated spectrogram was generated via Fast-Fourier Transform over 2048 data points using 50% overlap between windows, before converting the spectrum into dB-scale.

To assess the origin time of the most dominant *T* phases, we acquired seismic records of 14 sensors located across the SW Pacific (Fig. 1B). We applied a 1- to 10-Hz Butterworth bandpass filter to the raw data, before demeaning and detrending each trace. Spectra were generated using a 5-s rolling window with an overlap of 80%. We manually assessed spectra and waveforms to determine the arrival time of the *T* phase at each station (figs. S3 and S4). On the basis of the distance between each station and Hunga volcano, and assuming an average hydro-acoustic wave velocity of 1.49 km s^{-1}, we determined a hypothetical origin time for the main *T* phase recorded after 05:28. On the basis the earliest identified event time, we assessed the signal delay at the remaining stations (table S1). We repeated this process for the second main *T* wave on the same stations, with travel time for the NW stations well behaved but the SE stations recording late arrivals (figs. S5 and S6 and table S2). Note that the Niue seismic sensor (~600 km from Hunga) was not operational at the time of eruption. We used one-dimensional bathymetric profiles along the travel paths between Hunga volcano and each seismic sensor (fig. S8) as a preliminary assessment of the factors affecting signal dispersion. These profiles were generated from GEBCO (*76*) and Mitchel *et al.* (*77*) bathymetry maps via Q-GIS software.

Supplementary Materials

This PDF file includes:
Figs. S1 to S8
Tables S1 and S2

REFERENCES

1. J. L. Carr, Á. Horváth, D. L. Wu, M. D. Friberg, Stereo plume height and motion retrievals for the record-setting Hunga Tonga-Hunga Ha'apai eruption of 15 January 2022. *Geophys. Res. Lett.* **49**, e2022GL098131 (2022).
2. S. R. Proud, A. T. Prata, S. Schmauß, The January 2022 eruption of Hunga Tonga-Hunga Ha'apai volcano reached the mesosphere. *Science* **378**, 554–557 (2022).
3. A. R. Van Eaton, J. Lapierre, S. A. Behnke, C. Vagasky, C. J. Schultz, M. Pavolonis, K. Bedka, K. Khlopenkov, Lightning rings and gravity waves: Insights into the giant eruption plume from Tonga's Hunga Volcano on 15 January 2022. *Geophys. Res. Lett.* **50**, e2022GL102341 (2023).
4. P. Lynett, M. M. Cann, Z. Zhou, W. Renteria, J. Borrero, D. Greer, O. Fa'anunu, C. Bosserelle, B. Jaffe, S. P. La Selle, A. Ritchie, A. Snyder, B. Nasr, J. Bott, N. Graehl, C. Synolakis, B. Ebrahimi, G. E. Cinar, Diverse tsunamigenesis triggered by the Hunga Tonga-Hunga Ha'apai eruption. *Nature* **609**, 728–733 (2022).
5. C. J. Wright, N. P. Hindley, M. J. Alexander, M. Barlow, L. Hoffmann, C. N. Mitchell, F. Prata, M. Bouillon, J. Carstens, C. Clerbaux, S. Osprey, N. Powell, C. E. Randall, J. Yue, Surface-to-space atmospheric waves from Hunga Tonga–Hunga Ha'apai eruption. *Nature* **609**, 741–746 (2022).
6. E. A. Okal, Quantifying the ocean coupling of air waves, and why DART data reporting can be deceptive. *Pure Appl. Geophys.* **181**, 1095–1115 (2024).
7. J. Vergoz, P. Hupe, C. Listowski, A. Le Pichon, M. A. Garcés, E. Marchetti, P. Labazuy, L. Ceranna, C. Pilger, P. Gaebler, S. P. Näsholm, Q. Brissaud, P. Poli, N. Shapirio, R. De Negri, P. Mialle, IMS observations of infrasound and acoustic-gravity waves produced by the January 2022 volcanic eruption of Hunga, Tonga: A global analysis. *Earth Planet. Sci. Lett.* **591**, 117639 (2022).
8. M. A. Clare, I. A. Yeo, S. Watson, R. Wysoczanski, S. Seabrook, K. Mackay, J. E. Hunt, E. Lane, P. J. Talling, E. Pope, S. Cronin, M. Ribo, T. Kula, D. Tappin, S. Henrys, C. De Ronde,

M. Urlaub, S. Kutterolf, S. Fonua, S. Panuve, D. Veverka, R. Rapp, V. Kamalov, M. Williams, Fast and destructive density currents created by ocean-entering volcanic eruptions. *Science* **381**, 1085–1092 (2023).
9. H. Le Mével, C. A. Miller, M. Ribó, S. Cronin, T. Kula, The magmatic system under Hunga volcano before and after the 15 January 2022 eruption. *Sci. Adv.* **9**, eadh3156 (2023).
10. S. Seabrook, K. Mackay, S. J. Watson, M. A. Clare, J. E. Hunt, I. A. Yeo, E. M. Lane, M. R. Clark, R. Wysoczanski, A. A. Rowden, T. Kula, L. J. Hoffmann, E. Armstrong, M. J. M. Williams, Volcaniclastic density currents explain widespread and diverse seafloor impacts of the 2022 Hunga Volcano eruption. *Nat. Commun.* **14**, 7881 (2023).
11. S. J. Cronin, M. Ribó-Gene, M. Brenna, J. Wu, J. Paredes-Marino, E. Okal, J. D. L. White, S.-H. Park, M. A. Clare, I. A. Yeo, J.C. Borrero, B. Steinke, T. Kula, F. Latuila, P. Tuakafu, N. Heni, Multiproxy evidence for caldera collapse during the climactic phase of the 2022 Hunga eruption, Tonga, SW Pacific. *Chapman Conf. Caldera-Forming Eruptions Basaltic Volcanoes* (2025).
12. M. Carvajal, I. Sepúlveda, A. Gubler, R. Garreaud, Worldwide signature of the 2022 Tonga volcanic tsunami. *Geophys. Res. Lett.* **49**, e2022GL098153 (2022).
13. R. S. Matoza, D. Fee, J. D. Assink, A. M. Iezzi, D. N. Green, K. Kim, L. Toney, T. Lecocq, S. Krishnamoorthy, J. M. Lalande, K. Nishida, K. L. Gee, M. M. Haney, H. D. Ortiz, Q. Brissaud, L. Martire, L. Rolland, P. Vergados, A. Nippress, J. Park, S. Shani-Kadmiel, A. Witsil, S. Arrowsmith, C. Caudron, S. Watada, A. B. Perttu, B. Taisne, P. Mialle, A. le Pichon, J. Vergoz, P. Hupe, P. S. Blom, R. Waxler, S. de Angelis, J. B. Snively, A. T. Ringler, R. E. Anthony, A. D. Jolly, G. Kilgour, G. Averbuch, M. Ripepe, M. Ichihara, A. Arciniega-Ceballos, E. Astafyeva, L. Ceranna, S. Cevuard, I. Y. Che, R. de Negri, C. W. Ebeling, L. G. Evers, L. E. Franco-Marin, T. B. Gabrielson, K. Hafner, R. G. Harrison, A. Komjathy, G. Lacanna, J. Lyons, K. A. Macpherson, E. Marchetti, K. F. McKee, R. J. Mellors, G. Mendo-Pérez, T. D. Mikesell, E. Munaibari, M. Oyola-Merced, I. Park, C. Pilger, C. Ramos, M. C. Ruiz, R. Sabatini, H. F. Schwaiger, D. Tailpied, C. Talmadge, J. Vidot, J. Webster, D. C. Wilson, Atmospheric waves and global seismoacoustic observations of the January 2022 Hunga eruption. *Science* **377**, 95–100 (2022).
14. M. T. Ramírez-Herrera, O. Coca, V. Vargas-Espinosa, Tsunami effects on the Coast of Mexico by the Hunga Tonga-Hunga Ha'apai volcano eruption, Tonga. *Pure Appl. Geophys.* **179**, 1117–1137 (2022).
15. J. C. Borrero, S. J. Cronin, F. H. Latu'ila, P. Tukuafu, N. Heni, A. M. Tupou, T. Kula, O. Fa'anunu, C. Bosserelle, E. Lane, P. Lynett, L. Kong, Tsunami runup and inundation in Tonga from the January 2022 eruption of Hunga Volcano. *Pure Appl. Geophys.* **180**, 1–22 (2023).
16. S. J. Purkis, S. N. Ward, N. M. Fitzpatrick, J. B. Garvin, D. Slayback, S. J. Cronin, M. Palaseanu-Lovejoy, A. Dempsey, The 2022 Hunga-Tonga megatsunami: Near-field simulation of a once-in-a-century event. *Sci. Adv.* **9**, eadf5493 (2023).
17. F. Schindelé, L. Kong, E. M. Lane, R. Paris, M. Ripepe, V. Titov, R. Bailey, A review of tsunamis generated by volcanoes (TGV) source mechanism, modelling, monitoring and warning systems. *Pure Appl. Geophys.* **181**, 1745–1792 (2024).
18. V. K. Gusiakov, "Tsunami Impact on the African Continent: Historical Cases and Hazard Evaluation" in *Extreme Natural Hazards, Disaster Risks and Societal Implications* (Cambridge Univ. Press, 2014), pp. 225–233.
19. R. Paris, P. Wassmer, F. Lavigne, A. Belousov, M. Belousova, Y. Iskandarsyah, M. Benbakkar, B. Ontowirjo, N. Mazzoni, Coupling eruption and tsunami records: The Krakatau 1883 case study. Indonesia. *Bull. Volcanol.* **76**, 814 (2014).
20. F. Maeno, F. Imamura, Tsunami generation by a rapid entrance of pyroclastic flow into the sea during the 1883 Krakatau eruption, Indonesia. *J. Geophys. Res. Solid Earth* **116**, B09205 (2011).
21. R. Paris, Source mechanisms of volcanic tsunamis. *Phil. Trans. R. Soc. A* **373**, 20140380 (2015).
22. S. Falvard, R. Paris, M. Belousova, A. Belousov, T. Giachetti, S. Cuven, Scenario of the 1996 volcanic tsunamis in Karymskoye Lake, Kamchatka, inferred from X-ray tomography of heavy minerals in tsunami deposits. *Mar. Geol.* **396**, 160–170 (2018).
23. J. Karstens, C. Berndt, M. Urlaub, S. F. L. Watt, A. Micallef, M. Ray, I. Klaucke, S. Muff, D. Klaeschen, M. Kühn, T. Roth, C. Böttner, B. Schramm, J. Elger, S. Brune, From gradual spreading to catastrophic collapse–Reconstruction of the 1888 Ritter Island volcanic sector collapse from high-resolution 3D seismic data. *Earth Planet. Sci. Lett.* **517**, 1–13 (2019).
24. N. Lipiejko, C. N. Whittaker, E. M. Lane, J. D. White, W. L. Power, Tsunami generation by underwater volcanic explosions: Application to the 1952 explosions of Myojinsho Volcano. *Pure Appl. Geophys.* **178**, 4743–4761 (2021).
25. S. J. Cronin, M. Brenna, I. E. M. Smith, S. J. Barker, M. Tost, M. Ford, S. Tonga'onevai, T. Kula, R. Vaiomounga, New volcanic island unveils explosive past. *Eos* **98**, 1 (2017).
26. M. Brenna, S. J. Cronin, I. E. M. Smith, A. Pontesilli, M. Tost, S. Barker, S. Tonga'onevai, T. Kula, R. Vaiomounga, Post-caldera volcanism reveals shallow priming of an intra-ocean arc andesitic caldera: Hunga volcano, Tonga, SW Pacific. *Lithos* **412**, 106614 (2022).
27. N. Geshi, J. Ruch, V. Acocella, Evaluating volumes for magma chambers and magma withdrawn for caldera collapse. *Earth Planet. Sci. Lett.* **396**, 107–115 (2014).
28. O. Roche, T. H. Druitt, O. Merle, Experimental study of caldera formation. *J. Geophys. Res.* **105**, 395–416 (2000).
29. J. Cole, D. Milner, K. Spinks, Calderas and caldera structures: A review. *Earth Sci. Rev.* **69**, 1–26 (2005).
30. J. Stix, T. Kobayashi, Magma dynamics and collapse mechanisms during four historic caldera-forming events. *J. Geophys. Res.* **113**, B09205 (2008).
31. M. Ulvrova, R. Paris, P. Nomikou, K. Kelfoun, S. Leibrandt, D. R. Tappin, F. W. McCoy, Source of the tsunami generated by the 1650 AD eruption of Kolumbo submarine volcano (Aegean Sea, Greece). *J. Volcanol. Geotherm. Res.* **321**, 125–139 (2016).
32. N. Geshi, F. Maeno, S. Nakagawa, H. Naruo, T. Kobayashi, Tsunami deposits associated with the 7.3 ka caldera-forming eruption of the Kikai Caldera, insights for tsunami generation during submarine caldera-forming eruptions. *J. Volcanol. Geotherm. Res.* **347**, 221–233 (2017).
33. J. D. White, Subaqueous eruption-fed density currents and their deposits. *Precambrian Res.* **101**, 87–109 (2000).
34. A. G. Wech, M. M. Haney, J. C. Chang, A. D. Jolly, C. E. Yoon, R. J. Skoumal, Local, regional, and distal recordings of seismic unrest at Ta'ū Island volcano. American Samoa. *Bull. Volcanol.* **87**, 15 (2025).
35. J. A. Kintner, W. L. Yeck, P. S. Earle, S. Prejean, J. D. Pesicek, High-precision characterization of seismicity from the 2022 Hunga Tonga-Hunga Ha'apai volcanic eruption. *Seismol. Soc. Am.* **94**, 589–602 (2023).
36. J. Talandier, E. A. Okal, On the mechanism of conversion of seismic waves to and from *T* waves in the vicinity of island shores. *Bull. Seismol. Soc. Am.* **88**, 621–632 (1998).
37. M. Ewing, G. P. Woollard, A. C. Vine, J. L. Worzel, Recent results in submarine geophysics. *Geol. Soc. Am. Bull.* **57**, 909–934 (1946).
38. L. D. Leet, D. Linehan, P. R. Berger, Investigation of the *T* phase. *Bull. Seismol. Soc. Am.* **41**, 123–141 (1951).
39. E. A. Okal, The generation of *T* waves by earthquakes. *Adv. Geophys.* **49**, 1–65 (2008).
40. R. Heyburn, D. Bowers, D. N. Green, Seismic and hydroacoustic observations from recent underwater events in the South Atlantic Ocean. *Geophys. J. Int.* **223**, 289–300 (2020).
41. H. Kanamori, Mechanism of tsunami earthquakes. *Phys. Earth Planet. Inter.* **6**, 346–359 (1972).
42. E. A. Okal, *T* waves from the 1998 Papua New Guinea earthquake and its aftershocks: Timing the tsunamigenic slump. *Pure Appl. Geophys.* **160**, 1843–1863 (2003).
43. E. A. Okal, P.-J. Alasset, O. Hyvernaud, F. Schindelé, The deficient *T* waves of tsunami earthquakes. *Geophys. J. Int.* **152**, 416–432 (2003).
44. D. R. Bohnenstiehl, R. P. Dziak, H. Matsumoto, T.-K. A. Lau, Underwater acoustic records from the March 2009 eruption of Hunga Ha'apai-Hunga Tonga volcano in the Kingdom of Tonga. *J. Volcanol. Geotherm. Res.* **249**, 12–24 (2013).
45. D. R. Bohnenstiehl, R. P. Dziak, H. Matsumoto, J. A. Conder, Acoustic response of submarine volcanoes in the Tofua Arc and northern Lau Basin to two great earthquakes. *Geophys. J. Int.* **196**, 1657–1675 (2014).
46. A. Lavayssière, S. Bazin, J.-Y. Royer, Hydroacoustic monitoring of mayotte submarine volcano during its eruptive phase. *Geosciences* **14**, 170 (2024).
47. A. K. Gupta, R. Bennartz, K. E. Fauria, T. Mittal, Eruption chronology of the December 2021 to January 2022 Hunga Tonga-Hunga Ha'apai eruption sequence. *Commun. Earth Environ.* **3**, 314 (2022).
48. K. Tarumi, K. Yoshizawa, Eruption sequence of the 2022 Hunga Tonga-Hunga Ha'apai explosion from back-projection of teleseismic *P* waves. *Earth Planet. Sci. Lett.* **602**, 117966 (2023).
49. G. Harrison, Pressure anomalies from the January 2022 Hunga Tonga-Hunga Ha'apai eruption. *Weather* **77**, 87–90 (2022).
50. T. Kubota, T. Saito, K. Nishida, Global fast-traveling tsunamis driven by atmospheric Lamb waves on the 2022 Tonga eruption. *Science* **377**, 91–94 (2022).
51. J. Wu, S. J. Cronin, M. Brenna, S.-H. Park, A. Pontesilli, I. A. Ukstins, D. Adams, J. Paredes-Mariño, K. Hamilton, M. Huebsch, D. González-García, C. Firth, J. D. L. White, A. R. L. Nichols, T. Plank, J. Vongsvivut, A. Klein, F. Ramos, F. Latu'ila, T. Kula, Low sulfur emissions from 2022 Hunga eruption due to seawater–magma interactions. *Nat. Geosci.* **18**, 518–524 (2025).
52. L. G. Mastin, A. R. Van Eaton, S. J. Cronin, Did steam boost the height and growth of the giant Hunga eruption plume? *Bull. Volcanol.* **86**, 64 (2024).
53. M. Chaknova, T. Giachetti, J. Paredes-Mariño, A. Soule, A. R. Van Eaton, R. Beinart, M. Crundwell, S. J. Cronin, M. Jutzeler, K. E. Fauria, M. A. Clare, I. A. Yeo, S. Arellano, L. Kelly, S. Watson, R. Carey, T. Kula, C. M. Young, How did westward volcaniclastic deposits accumulate in the deep sea following the January 2022 eruption of Hunga Volcano? *Geochem. Geophys. Geosyst.* **26**, e2024GC011629 (2025).
54. A. Clarke, B. Voight, A. Neri, G. Macedonio, Transient dynamics of vulcanian explosions and column collapse. *Nature* **415**, 897–901 (2002).
55. Y. J. Suzuki, T. Koyaguchi, 3-D numerical simulations of eruption column collapse: Effects of vent size on pressure-balanced jet/plumes. *J. Volcanol. Geotherm. Res.* **221**, 1–13 (2012).
56. G. Carazzo, E. Kaminski, S. Tait, The timing and intensity of column collapse during explosive volcanic eruptions. *Earth Planet. Sci. Lett.* **411**, 208–217 (2015).
57. T. Koyaguchi, Y. J. Suzuki, K. Takeda, S. Inagawa, The condition of eruption column collapse: 2. Three-dimensional numerical simulations of eruption column dynamics. *J. Geophys. Res. Solid Earth* **123**, 7483–7508 (2018).

58. A. Van Eaton, M. Herzog, C. Wilson, J. McGregor, Ascent dynamics of large phreatomagmatic eruption clouds: The role of microphysics. *J. Geophys. Res. Solid Earth* **117**, B03203 (2012).
59. V. Acocella, Understanding caldera structure and development: An overview of analogue models compared to natural calderas. *Earth Sci. Rev.* **85**, 125–160 (2007).
60. A. Folch, J. Martí, Time-dependent chamber and vent conditions during explosive caldera-forming eruptions. *Earth Planet. Sci. Lett.* **280**, 246–253 (2009).
61. N. Geshi, I. Miyagi, G. Saito, C. E. Conway, Caldera collapse thresholds correlate with magma chamber dimensions. *Sci. Rep.* **13**, 7463 (2023).
62. F. Maeno, F. Imamura, H. Taniguchi, Numerical simulation of tsunamis generated by caldera collapse during the 7.3 ka Kikai eruption, Kyushu, Japan. *Earth Planets Space* **58**, 1013–1024 (2006).
63. E. L. Geist, Phenomenology of tsunamis: Statistical properties from generation to runup. *Adv. Geophys.* **51**, 107–169 (2009).
64. E. A. Okal, C. E. Synolakis, Sequencing of tsunami waves: Why the first wave is not always the largest. *Geophys. J. Int.* **204**, 719–735 (2016).
65. J. C. Borrero, T. Soilhuddin, Field survey and numerical modelling of the December 22, 2018 Anak Krakatau tsunami. *Pure Appl. Geophys.* **177**, 2457–2475 (2020).
66. J. L. Latchman, F. J.-Y. Dondin, R. E. A. Robertson, R. Stewart, P. Smith, L. L. Lynch, C. Ramsingh, N. Hath, H. Ramsingh, I. Juman, S. Edwards, C. Ash, Contrasting *T*-phase and *P*-wave patterns from the 2015 and 2017 eruptions of the submarine volcano Kick-'em-Jenny: Influence of cardinal direction on recorded first phase arrival. *Bull. Seismol. Soc. Am.* **113**, 2056–2068 (2023).
67. S. Thorarinsson, T. Einarsson, G. Sigvaldason, G. Elisson, The submarine eruption off the Vestmann islands 1963–64: A preliminary report. *Bull. Volcanol.* **27**, 435–445 (1964).
68. K. Németh, S. J. Cronin, D. Charley, M. Harrison, E. Garae, Exploding lakes in Vanuatu—"Surtseyan-style" eruptions witnessed on Ambae Island. *Episodes* **29**, 87–92 (2006).
69. C. F. Waythomas, L. G. Mastin, Mechanisms for ballistic block ejection during the 2016–2017 shallow submarine eruption of Bogoslof volcano. Alaska. *Bull. Volcanol.* **82**, 13 (2020).
70. F. Maeno, T. Kaneko, M. Ichihara, Y. J. Suzuki, A. Yasuda, K. Nishida, T. Ohminato, Seawater-magma interactions sustained the high column during the 2021 phreatomagmatic eruption of Fukutoku-Oka-no-Ba. *Commun. Earth Environ.* **3**, 260 (2022).
71. T. C. Oliveira, Y.-T. Lin, N. Kushida, S. M. Jesus, P. Nielsen, *T*-wave propagation from the Pacific to the Atlantic: The 2020 Mw7. 4 Kermadec Trench earthquake case. *JASA Express Lett.* **1**, 126001 (2021).
72. T. C. Oliveira, P. Nielsen, Y.-T. Lin, N. Kushida, S. M. Jesus, Megameter propagation and correlation of *T*-waves from Kermadec Trench and Islands. *Front. Mar. Sci.* **9**, 1009013 (2022).
73. E. Okal, O. Hyvernaud, A. Paris, H. Hebert, P. Heinrich, "Ancillary records of the Krakatau eruption and tsunami of 22 December 2018" in *EGU General Assembly 2019* (EGU, 2019), abstr. EGU2019–11563.
74. C. E. Synolakis, J.-P. Bardet, J. C. Borrero, H. L. Davies, E. A. Okal, E. A. Silver, S. Sweet, D. R. Tappin, The slump origin of the 1998 Papua New Guinea tsunami. *Proc. R. Soc. A: Math. Phys. Eng. Sci.* **458**, 763–789 (2002).
75. S. Takemura, T. Kubota, O. Sandanbata, Successive tsunamigenic events near Sofu Seamount inferred from high-frequency teleseismic *P* and regional *T* waves. *J. Geophys. Res. Solid Earth* **129**, e2024JB029746 (2024).
76. GEBCO Compilation Group, GEBCO 2024 Grid (doi:10.5285/1c44ce99-0a0d-5f4f-e063-7086abc0ea0f) (2024).
77. J. S. Mitchell, K. Mackay, H. Neil, A. Pallentin, P. Notman, Undersea New Zealand, 1:5,000,000. *NIWA Chart, Misc. Ser.* **92**, 725 (2012).

Acknowledgments: We are grateful to the many Tongan families and colleagues who supported our field work, hosted us, and provided valuable interviews, photographs, and video recordings during this study. **Funding:** This work was supported by the New Zealand Government Ministry of Business Innovation and Employment Endeavour Research Programme UOA24103 (S.J.C.) and Korean Polar Research Institute PE22550 and PE26050 (S.-H.P.). **Author contributions:** Conceptualization: S.J.C. Field work: S.J.C., J.C.B., R.V., T.K., and S.-H.P. Investigation: S.J.C., M.R., M.B., J.W., J.P.-M., M.H., R.B., U.S., R.V., T.K., and S.-H.P. Formal analysis and methodology: S.J.C. (overall), B.S., E.A.O. (seismic), J.C.B. (tsunami), A.R.V.E., and L.G.M. (plume). Visualization: S.J.C., B.S., and M.R. Funding acquisition: S.J.C., M.R., S.-H.P., and M.B. Discussion: all authors; Writing–original draft: S.J.C., B.S., and E.O. Writing–review and editing: all authors. **Competing interests:** The authors declare that they have no competing interests. **Data, code, and materials availability:** All data needed to evaluate and reproduce the results in the paper are present in the paper and/or the Supplementary Materials. This study did not generate new materials. All codes used are described and are open-access and the seismic station information is available at the international repositories listed in the Supplementary Materials.

Submitted 29 October 2025
Accepted 24 July 2026
Published 2 September 2026
10.1126/sciadv.aed4934

Science Advances

Delayed submarine caldera subsidence creates extreme tsunami hazard

Shane J. Cronin, Bastian Steinke, Jose C. Borrero, Emile A. Okal, Marta Ribó, Jie Wu, James D. L. White, Marco Brenna, Joali Paredes-Mariño, Mila Huebsch, Rachael Baxter, Ulrich Speidel, Alexa R. Van Eaton, Larry G. Mastin, Michael A. Clare, Isobel A. Yeo, James E. Hunt, Jacob Nash, James B. Garvin, Rennie Vaiomounga, Taaniela Kula, and Sung-Hyun Park

Sci. Adv. **12** (36), eaed4934. DOI: 10.1126/sciadv.aed4934

Science Advances (ISSN 2375-2548) is published by the American Association for the Advancement of Science. 1200 New York Avenue NW, Washington, DC 20005. The title *Science Advances* is a registered trademark of AAAS.